Publication Year	2022
Acceptance in OA	2025-02-26T16:48:44Z
Title	Weak Mass Loss from the Red Supergiant Progenitor of the Type II SN 2021yja
Authors	Hosseinzadeh, Griffin, Kilpatrick, Charles D., Dong, Yize, Sand, David J., Andrews, Jennifer E., Bostroem, K. Azalee, Janzen, Daryl, Jencson, Jacob E., Lundquist, Michael, Meza Retamal, Nicolas E., Pearson, Jeniveve, Valenti, Stefano, Wyatt, Samuel, Burke, Jamison, Hiramatsu, Daichi, Howell, D. Andrew, McCully, Curtis, Newsome, Megan, Gonzalez, Estefania Padilla, Pellegrino, Craig, Terreran, Giacomo, Auchettl, Katie, Davis, Kyle W., Foley, Ryan J., Miao, Hao-Yu, Pan, Yen-Chen, Rest, Armin, Siebert, Matthew R., Taggart, Kirsty, Tucker, Brad E., Cyrus Leung, Feng Lin, Swift, Jonathan J., Yang, Grace, Anderson, Joseph P., Ashall, Chris, BENETTI, Stefano, Brown, Peter J., Cartier, Régis, Chen, Ting-Wan, DELLA VALLE, Massimo, Galbany, Lluís, Gomez, Sebastian, Gromadzki, Mariusz, Haislip, Joshua, Hsiao, Eric Y., Inserra, Cosimo, Jha, Saurabh W., Killestein, Thomas L., Kouprianov, Vladimir, Kozyreva, Alexandra, Müller-Bravo, Tomás E., Nicholl, Matt, Paraskeva, Emmy, Reichart, Daniel E., Ryder, Stuart, Shahbandeh, Melissa, Shappee, Ben, Smith, Nathan, Young, David R.
Publisher's version (DOI)	10.3847/1538-4357/ac75f0
Handle	http://hdl.handle.net/20.500.12386/36294
Journal	THE ASTROPHYSICAL JOURNAL
Volume	935

The Astrophysical Journal, 935:31 (24pp), 2022 August 10 https://doi.org/10.3847/1538-4357/ac75f0

Weak Mass Loss from the Red Supergiant Progenitor of the Type II SN 2021yja

Griffin Hosseinzadeh[1], Charles D. Kilpatrick[2], Yize Dong (董一泽)[3], David J. Sand[1], Jennifer E. Andrews[4], K. Azalee Bostroem[5,46], Daryl Janzen[6], Jacob E. Jencson[1], Michael Lundquist[7], Nicolas E. Meza Retamal[3], Jeniveve Pearson[1], Stefano Valenti[3], Samuel Wyatt[1], Jamison Burke[8,9], Daichi Hiramatsu[10,11], D. Andrew Howell[8,9], Curtis McCully[8,9], Megan Newsome[8,9], Estefania Padilla Gonzalez[8,9], Craig Pellegrino[8,9], Giacomo Terreran[8,9], Katie Auchettl[12,13,14], Kyle W. Davis[14], Ryan J. Foley[14], Hao-Yu Miao (繆皓宇)[15], Yen-Chen Pan (潘彥丞)[15], Armin Rest[16,17], Matthew R. Siebert[14], Kirsty Taggart[14], Brad E. Tucker[13,18,19], Feng Lin Cyrus Leung[20], Jonathan J. Swift[20], Grace Yang[20], Joseph P. Anderson[21], Chris Ashall[22], Stefano Benetti[23], Peter J. Brown[24,25], Régis Cartier[26], Ting-Wan Chen (陳婷琬)[27], Massimo Della Valle[28,29,30], Lluís Galbany[31,32], Sebastian Gomez[16], Mariusz Gromadzki[33], Joshua Haislip[34], Eric Y. Hsiao[35], Cosimo Inserra[36], Saurabh W. Jha[37], Thomas L. Killestein[38], Vladimir Kouprianov[34], Alexandra Kozyreva[39], Tomás E. Müller-Bravo[31], Matt Nicholl[40], Emmy Paraskeva[41,42], Daniel E. Reichart[34], Stuart Ryder[43,44], Melissa Shahbandeh[35], Ben Shappee[22], Nathan Smith[1], and David R. Young[45]

[1] Steward Observatory, University of Arizona, 933 North Cherry Avenue, Tucson, AZ 85721-0065, USA; griffin0@arizona.edu
[2] Center for Interdisciplinary Exploration and Research in Astrophysics and Department of Physics and Astronomy, Northwestern University, 1800 Sherman Avenue, 8th Floor, Evanston, IL 60201, USA
[3] Department of Physics and Astronomy, University of California, Davis, 1 Shields Avenue, Davis, CA 95616-5270, USA
[4] Gemini Observatory, 670 North A'ohoku Place, Hilo, HI 96720-2700, USA
[5] Department of Astronomy, University of Washington, 3910 15th Avenue NE, Seattle, WA 98195-0002, USA
[6] Department of Physics & Engineering Physics, University of Saskatchewan, 116 Science Place, Saskatoon, SK S7N 5E2, Canada
[7] W.M. Keck Observatory, 65-1120 Māmalahoa Highway, Kamuela, HI 96743-8431, USA
[8] Las Cumbres Observatory, 6740 Cortona Drive, Suite 102, Goleta, CA 93117-5575, USA
[9] Department of Physics, University of California, Santa Barbara, CA 93106-9530, USA
[10] Center for Astrophysics | Harvard & Smithsonian, 60 Garden Street, Cambridge, MA 02138-1516, USA
[11] The NSF AI Institute for Artificial Intelligence and Fundamental Interactions, USA
[12] School of Physics, The University of Melbourne, Parkville, VIC 3010, Australia
[13] ARC Centre of Excellence for All Sky Astrophysics in 3 Dimensions (ASTRO 3D), Australia
[14] Department of Astronomy and Astrophysics, University of California, Santa Cruz, CA 95064-1077, USA
[15] Graduate Institute of Astronomy, National Central University, 300 Jhongda Road, 32001 Jhongli, Taiwan
[16] Space Telescope Science Institute, 3700 San Martin Drive, Baltimore, MD 21218-2410, USA
[17] Department of Physics and Astronomy, The Johns Hopkins University, 3400 North Charles Street, Baltimore, MD 21218, USA
[18] Mt. Stromlo Observatory, The Research School of Astronomy and Astrophysics, Australian National University, ACT 2601, Australia
[19] National Centre for the Public Awareness of Science, Australian National University, Canberra, ACT 2611, Australia
[20] Thacher School, 5025 Thacher Road, Ojai, CA 93023-8304, USA
[21] European Southern Observatory, Alonso de Córdova 3107, Casilla 19, Santiago, Chile
[22] Institute for Astronomy, University of Hawai'i, 2680 Woodlawn Drive, Honolulu, HI 96822-1839, USA
[23] INAF—Osservatorio Astronomico di Padova, Vicolo dell'Osservatorio 5, I-35122 Padova, Italy
[24] Department of Physics and Astronomy, Texas A&M University, 4242 TAMU, College Station, TX 77843, USA
[25] George P. and Cynthia Woods Mitchell Institute for Fundamental Physics & Astronomy, College Station, TX 77843, USA
[26] Gemini Observatory, NSF's National Optical-Infrared Astronomy Research Laboratory, Casilla 603, La Serena, Chile
[27] Oskar Klein Centre, Department of Astronomy, Stockholm University, Albanova University Centre, SE-106 91 Stockholm, Sweden
[28] INAF—Capodimonte Astronomical Observatory, Salita Moiariello 16, I-80131 Napoli, Italy
[29] INFN—Napoli, Strada Comunale Cinthia, I-80126 Napoli, Italy
[30] ICRANet, Piazza della Repubblica 10, I-65122 Pescara, Italy
[31] Institute of Space Sciences (ICE, CSIC), Campus UAB, Carrer de Can Magrans, s/n, E-08193 Barcelona, Spain
[32] Institut d'Estudis Espacials de Catalunya, Gran Capità, 2-4, Edifici Nexus, Desp. 201, E-08034 Barcelona, Spain
[33] Astronomical Observatory, University of Warsaw, Al. Ujazdowskie 4, 00-478 Warszawa, Poland
[34] Department of Physics and Astronomy, University of North Carolina, 120 East Cameron Avenue, Chapel Hill, NC 27599, USA
[35] Department of Physics, Florida State University, 77 Chieftan Way, Tallahassee, FL 32306-4350, USA
[36] Cardiff Hub for Astrophysics Research and Technology, School of Physics & Astronomy, Cardiff University, Queens Buildings, The Parade, Cardiff, CF24 3AA, UK
[37] Department of Physics and Astronomy, Rutgers, the State University of New Jersey, 136 Frelinghuysen Road, Piscataway, NJ 08854-8019, USA
[38] Department of Physics, University of Warwick, Gibbet Hill Road, Coventry CV4 7AL, UK
[39] Max-Planck-Institut für Astrophysik, Karl-Schwarzschild-Straße 1, D-85748 Garching, Germany
[40] Birmingham Institute for Gravitational Wave Astronomy and School of Physics and Astronomy, University of Birmingham, Birmingham B15 2TT, UK
[41] IAASARS, National Observatory of Athens, 15236 Penteli, Greece
[42] Department of Astrophysics, Astronomy & Mechanics, Faculty of Physics, National and Kapodistrian University of Athens, 15784 Athens, Greece
[43] School of Mathematical and Physical Sciences, Macquarie University, NSW 2109, Australia
[44] Astronomy, Astrophysics and Astrophotonics Research Centre, Macquarie University, Sydney, NSW 2109, Australia
[45] Astrophysics Research Centre, School of Mathematics and Physics, Queen's University Belfast, Belfast BT7 1NN, UK
Received 2022 March 15; revised 2022 May 24; accepted 2022 May 30; published 2022 August 10

[46] DiRAC Fellow.

Abstract

We present high-cadence optical, ultraviolet (UV), and near-infrared data of the nearby ($D \approx 23$ Mpc) Type II supernova (SN) 2021yja. Many Type II SNe show signs of interaction with circumstellar material (CSM) during the first few days after explosion, implying that their red supergiant (RSG) progenitors experience episodic or eruptive mass loss. However, because it is difficult to discover SNe early, the diversity of CSM configurations in RSGs has not been fully mapped. SN 2021yja, first detected within ≈ 5.4 hours of explosion, shows some signatures of CSM interaction (high UV luminosity and radio and x-ray emission) but without the narrow emission lines or early light-curve peak that can accompany CSM. Here we analyze the densely sampled early light curve and spectral series of this nearby SN to infer the properties of its progenitor and CSM. We find that the most likely progenitor was an RSG with an extended envelope, encompassed by low-density CSM. We also present archival Hubble Space Telescope imaging of the host galaxy of SN 2021yja, which allows us to place a stringent upper limit of $\lesssim 9\,M_{\odot}$ on the progenitor mass. However, this is in tension with some aspects of the SN evolution, which point to a more massive progenitor. Our analysis highlights the need to consider progenitor structure when making inferences about CSM properties, and that a comprehensive view of CSM tracers should be made to give a fuller view of the last years of RSG evolution.

Unified Astronomy Thesaurus concepts: Circumstellar matter (241); Core-collapse supernovae (304); Stellar mass loss (1613); Supernovae (1668); Type II supernovae (1731)

Supporting material: data behind figures, machine-readable table

1. Introduction

Mass loss in massive stars ($M_{\rm ZAMS} \gtrsim 8\,M_{\odot}$) is among the most poorly understood aspects of stellar evolution (Smith 2014), and core-collapse supernovae (CCSNe) provide a complementary window into studying mass-loss processes that the stars of the Milky Way and its satellites cannot provide. In the case of pre-SN mass loss, the difficulty lies in the fact that mass-loss rates may change quickly, in which case the SN must be observed very shortly after explosion in order to map out the prognenitor's mass-loss history. For this reason, CCSNe in nearby galaxies—where early discovery, dense time sampling, and rich multiwavelength data sets are possible—offer a valuable opportunity for a mass-loss case study.

Type II supernovae (SNe II),[47] the most common CCSNe (Li et al. 2011; Smith et al. 2011), are the hydrogen-rich explosions of red supergiant (RSG) stars. This has been confirmed by the direct detection of tens of SN II progenitors in archival Hubble Space Telescope (HST) imaging (Smartt 2015; Van Dyk 2016). Traditionally, RSGs were not thought to produce detectable amounts of CSM, but recent work has shown that CSM is nearly ubiquitous in SN II progenitors and can affect the SN observables, particularly during the first days to weeks after explosion. For example, very early spectroscopy has revealed narrow emission lines from high-ionization states, interpreted as forming in the excited but unshocked CSM (Gal-Yam et al. 2014; Smith et al. 2015; Khazov et al. 2016; Yaron et al. 2017; Bullivant et al. 2018; Hosseinzadeh et al. 2018; Soumagnac et al. 2020; Bruch et al. 2021; Hiramatsu et al. 2021b; Terreran et al. 2022). Khazov et al. (2016) and Bruch et al. (2021) have observed these in a large fraction of SNe II. Likewise, Morozova et al. (2017, 2018) show through radiation-hydrodynamical modeling that early SN II light curves require a CSM component to reproduce the fast rise and sometimes even an early peak (see also González-Gaitán et al. 2015; Förster et al. 2018).

Given that both of these CSM signatures disappear shortly after explosion, early discovery, classification, and follow-up are critical to understanding circumstellar interaction in CCSNe, and therefore to understanding mass loss in CCSN progenitors. Specialized surveys like the Distance Less Than 40 Mpc (DLT40) Survey (Tartaglia et al. 2018) observe nearby galaxies frequently (twice per day for DLT40 in the southern hemisphere) with the goal of discovering new transients shortly after explosion, when they are still very faint, and announce discoveries immediately so that spectroscopic classification can occur shortly after. Such projects, used in concert with wide-field transient searches such as the Asteroid Terrestrial-impact Last Alert System (ATLAS; Tonry et al. 2018b), the Young Supernova Experiment (YSE; Jones et al. 2021), the All-Sky Automated Survey for Supernovae (Shappee et al. 2014), and the Zwicky Transient Facility (Bellm et al. 2019), can place strong limits on the explosion epochs of nearby SNe and allow for the most comprehensive early data sets to be acquired. Likewise, rapid robotic follow-up with facilities like Las Cumbres Observatory (Brown et al. 2013) and the Neil Gehrels Swift Observatory (Gehrels et al. 2004) allow us to trace the SN ejecta in detail as it collides with and overruns the material ejected in the years before explosion.

Here we consider the case of SN 2021yja, a nearby ($D \approx 23$ Mpc) SN II observed within hours of explosion and followed extensively in the optical and ultraviolet (UV) for the first 150 days of its evolution. The site of SN 2021yja was previously observed with HST to a depth that allows us to place a very strong constraint on the progenitor luminosity. In Section 2, we describe the discovery and observations of SN 2021yja and derive the properties of its host galaxy required for our analysis. In Section 3, we analyze the light curves, spectra, and pre-explosion imaging of SN 2021yja in order to constrain its progenitor properties, including the presence of any CSM, and we compare it to other well-observed SNe II in the literature. Finally, in Section 4, we discuss the implications of our measurements for the population of SN II progenitors and RSGs in general, with a focus on mass-loss histories.

2. Observations and Data Reduction

2.1. Discovery and Classification

SN 2021yja was discovered by ATLAS on 2021-09-08.55 (all dates are in UTC) at $c = 15.334 \pm 0.007$ mag and was not detected on 2021-09-06.48 to a 3σ limit of $o > 19.22$ mag

[47] Throughout this work, we use "SNe II" to refer to Type IIP and Type IIL SNe (Barbon et al. 1979), but not Type IIb or Type IIn SNe.

(Smith et al. 2021; Tonry et al. 2021). Its J2000 coordinates, as measured by Gaia Photometric Science Alerts, are $\alpha = 03^{h}24^{m}21^{s}.180$, $\delta = -21°33'56''.20$ (Hodgkin et al. 2021), 99″ southwest of the center of its host galaxy, NGC 1325.[48] It was recovered in earlier unfiltered (357–871 nm) imaging by the DLT40 Survey on 2021-09-08.29 at 16.431 ± 0.028 mag and was not detected on 2021-09-07.28 to a 3σ limit of 18.671 mag. Kilpatrick (2021) also recovered it at $g = 20.4 \pm 0.2$ mag and $r = i = 20.7 \pm 0.2$ mag in publicly available imaging taken on 2021-09-07.63 with the Multicolor Simultaneous Camera for Studying Atmospheres of Transiting Exoplanets 3 (MuSCAT3) on Las Cumbres Observatory's 2 m Faulkes Telescope North (Narita et al. 2020), taken as part of the Faulkes Telescope Project's education and public outreach program.[49] The very low luminosities implied by these magnitudes meant that it was not clear in real time whether these MuSCAT3 images were taken before or after explosion (see Section 3.2).

SN 2021yja was initially classified as a young SN II by Pellegrino et al. (2021) using a spectrum taken by the Global Supernova Project (GSP) on 2021-09-09.51, 15 hours after the ATLAS discovery report. Their classification was based on spectroscopic comparisons with other SNe II using Superfit (Howell et al. 2005) and the Supernova Identification code (SNID; Blondin & Tonry 2007). Shortly afterward, it was reclassified as a young stripped-envelope SN by Williamson et al. (2021) using a second spectrum taken by the GSP on 2021-09-09.60. They argued that the spectrum also resembled other young SN Ic spectra, and that the putative high-velocity Hα line could have been misidentified silicon 635.5 nm. Several days later, after stronger hydrogen lines had developed, Deckers et al. (2021a, 2021b) restored the SN II classification using a spectrum taken on 2021-09-14.31 by the advanced extended Public ESO Spectroscopic Survey of Transient Objects (ePESSTO+; Smartt et al. 2015).

2.2. Follow-up Photometry and Spectroscopy

We obtained UV, optical, and infrared photometry of SN 2021yja using the Sinistro cameras on Las Cumbres Observatory's network of 1 m telescopes (Brown et al. 2013),[50] MuSCAT3 on Las Cumbres Observatory's 2 m Faulkes Telescope North (Narita et al. 2020), an Andor iKON-L 936 BV camera on the 0.7 m telescope at Thacher Observatory (Swift et al. 2022), KeplerCam on the 1.2 m telescope at F. L. Whipple Observatory (Szentgyorgyi et al. 2005), the Lulin Compact Imager on the 1 m telescope at Lulin Observatory, the MMT and Magellan Infrared Spectrograph (MMIRS) on the MMT (McLeod et al. 2012), the Direct Imaging Camera on the Nickel Telescope (Stone & Shields 1990), the Ultraviolet/Optical Telescope on Swift (Roming et al. 2005), and Andor Apogee Alta F47 cameras on the Panchromatic Robotic Optical Monitoring and Polarimetry Telescopes at Cerro Tololo Inter-American Observatory and Meckering Observatory (Reichart et al. 2005) as part of the DLT40 Survey. See Appendix A for details of the photometry reduction. We also include publicly available photometry from the ATLAS forced photometry server (Tonry et al. 2018a; Smith et al. 2020) and the Supernova Observations and Simulations group (Martinez et al. 2021). Figure 1 shows the light curve of SN 2021yja; the data are available in machine-readable format in the online journal.

In addition, we obtained high-resolution follow-up imaging with the Gemini South Adaptive Optics Imager (GSAOI) at Cerro Pachón, Chile (McGregor et al. 2004). We observed the site of SN 2021yja on 2021-12-18 in *H*-band using an on-off pattern for 300 s of total on-source exposure. Following procedures in Kilpatrick et al. (2021), we performed image calibration using dark and flat-field frames obtained in the instrumental configuration.

After classification, we initiated a high-cadence optical spectroscopic follow-up campaign using the FLOYDS instruments on Las Cumbres Observatory's 2 m Faulkes Telescopes North and South (FTN & FTS; Brown et al. 2013), Binospec on the MMT (Fabricant et al. 2019), the Wide Field Spectrograph (WiFeS) on the 2.3 m telescope at Siding Spring Observatory (SSO; Dopita et al. 2007, 2010), the ESO Faint Object Spectrograph and Camera 2 (EFOSC2) on the New Technology Telescope (NTT; Buzzoni et al. 1984); the Keck Cosmic Web Imager (KCWI) on Keck II (Morrissey et al. 2018), the Robert Stobie Spectrograph (RSS) on the South African Large Telescope (SALT; Smith et al. 2006), the Kast Spectrograph on the Shane Telescope (Miller & Stone 1994), the Boller & Chivens Spectrograph (B&C) on the Bok Telescope (Green et al. 1995), the High-Resolution Echelle Spectrometer (HIRES) on Keck I (Vogt et al. 1994), the Goodman High Throughput Spectrograph on the Southern Astrophysical Research Telescope (SOAR; Clemens et al. 2004), and the Dual Imaging Spectrograph (DIS) on the Astrophysical Research Consortium (ARC) 3.5 m telescope (Lupton 2005). Figure 2 compares the earliest spectra of SN 2021yja, taken within 6 days of estimated explosion, to other early spectra of SNe II from Yaron et al. (2017); Andrews et al. (2019); Hiramatsu et al. (2021b); Tartaglia et al. (2021), and Terreran et al. (2022). The remaining optical spectra are plotted in Figure 3. We also obtained near-infrared spectra using the Near-Infrared Echelette Spectrometer (NIRES) on Keck II (Wilson et al. 2004), the Son of ISAAC spectrograph (SOFI) on the NTT (Moorwood et al. 1998), TripleSpec 4.1 on SOAR (Schlawin et al. 2014), and MMIRS on the MMT, which are plotted in Figure 4. All spectra were either observed at the parallactic angle, or an atmospheric dispersion corrector was used. Details of the spectroscopic reductions are given in Appendix B.

2.3. Pre-explosion Imaging

NGC 1325 and the site of SN 2021yja were observed by HST on 1997-03-26 with the Wide Field Planetary Camera 2 (WFPC2) in F606W (PI Stiavelli, SNAP-6359). We reduced all `c0m` frames with the `hst123` reduction pipeline and performed final photometry in the `c0m` frames using `dolphot`. In addition, we obtained DECam *grizY* imaging taken between 2014 and 2019 and covering the site of SN 2021yja. We stacked and calibrated all such data using a custom pipeline based on the `photpipe` imaging and photometry package (Rest et al. 2005). Finally, we downloaded pre-explosion Spitzer/IRAC imaging (Fazio et al. 2004; Werner et al. 2004; Gehrz et al. 2007) from the Spitzer Heritage Archive and combined the basic calibrated data

[48] NGC 1325 previously hosted SN 1975S, which was not spectroscopically classified (Wegner 1977).
[49] After a final reduction of these images, we report updated magnitudes in Figure 1 and its associated online-only table.
[50] Sinistro data were obtained under both the GSP and the YSE programs.

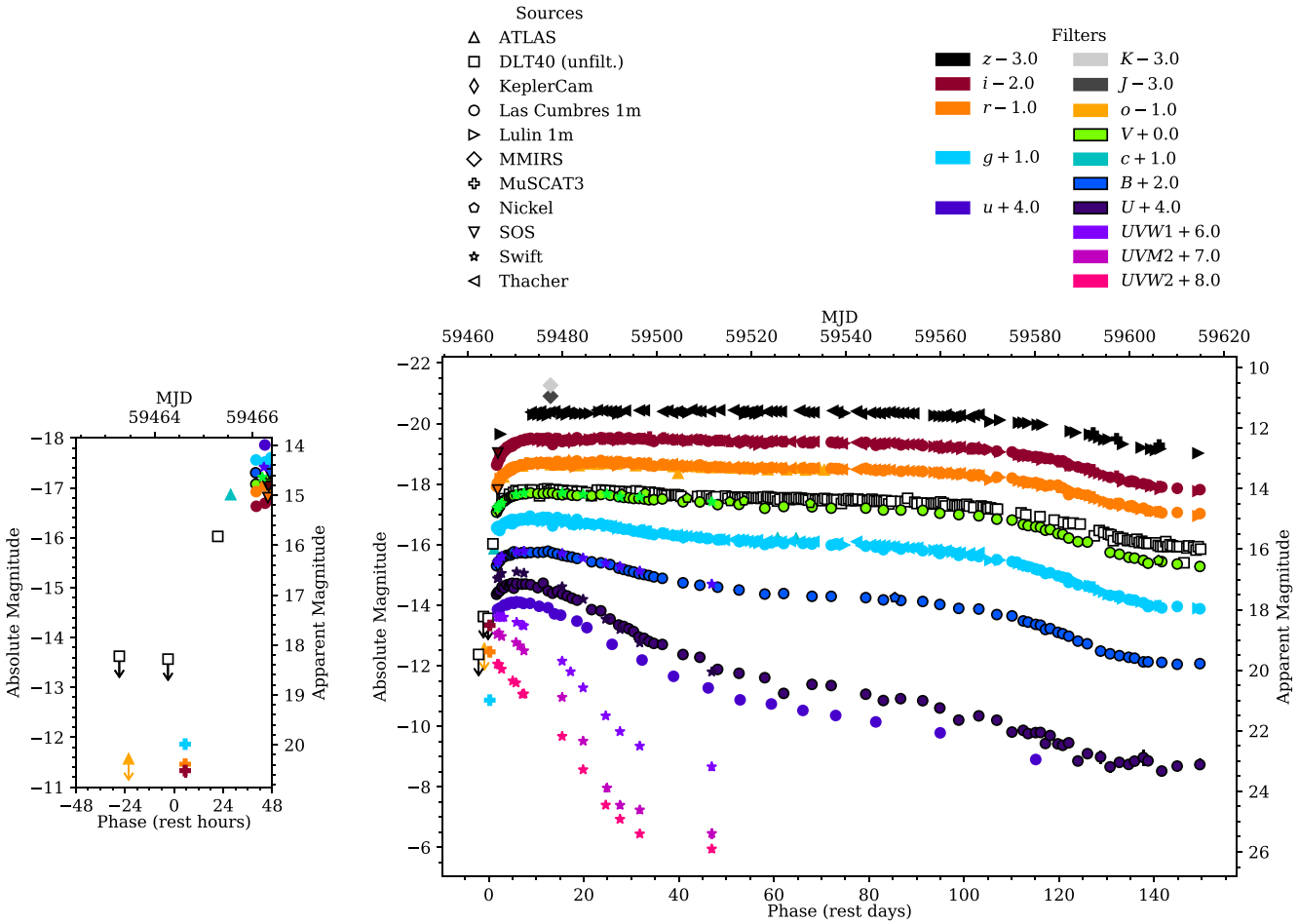

Figure 1. The main figure (right) shows the multiband UV-optical-infrared light curve of SN 2021yja through the end of its plateau. Phase is given in rest-frame days after estimated explosion. Note the unusually long (≈ 140 days) plateau and slow fall onto the radioactive-decay-powered tail (the last 3 epochs). The inset (left) shows the light curve within 48 hours of explosion, with no filter offsets. In particular, note the MuSCAT3 data (plus signs), which constrains the explosion epoch even more tightly than the nondetections by ATLAS and DLT40 (see Section 3.2).

(The data used to create this figure are available.)

(cbcd) frames following methods described in Kilpatrick et al. (2021). These pre-explosion data are analyzed in Section 3.5.

2.4. Redshift

NGC 1325 has a heliocentric redshift of $z = 0.005307 \pm 0.000005$ (Springob et al. 2005). However, we observe a weak, narrow Hα emission line in our Keck HIRES spectrum at a redshift of $z = 0.00568$, corresponding to a line-of-sight velocity of $c\Delta z = +112\,\mathrm{km\,s^{-1}}$ with respect to the galaxy core. This velocity is reasonable given the position of the SN and a typical galaxy rotation curve (Falcón-Barroso et al. 2017; Guidi et al. 2018), so we adopt this as the SN redshift.

2.5. Extinction

The equivalent widths of Na I D absorption lines have been shown to correlate with extinction due to interstellar dust (Richmond et al. 1994; Munari & Zwitter 1997). In order to measure the extinction in the direction of SN 2021yja, we examine the Na I D features in our Keck HIRES spectrum (pixel scale $\Delta x \approx 0.0026$ nm in the regions of interest), shown in Figure 5. The spectrum reveals four distinct absorption systems at $z = 0.00002$ (Milky Way), 0.00559, 0.00566, and 0.00568.

We measure the equivalent widths of each of these eight lines by fitting and integrating a Gaussian profile, resulting in the values shown in Table 1. (For the systems at $z = 0.00566$ and 0.00568, we simultaneously fit two Gaussian profiles.) We then convert these equivalent widths to $E(B-V)$ using Eq. (9) of Poznanski et al. (2012) and applying the renormalization factor of 0.86 from Schlafly et al. (2010). The Milky Way extinction value, $E(B-V)_{\mathrm{MW}} = 0.0152^{+0.0031}_{-0.0026}$ mag, is consistent with the value from Schlafly & Finkbeiner (2011), $E(B-V)_{\mathrm{MW}} = 0.0191$ mag. We adopt the latter. The host galaxy extinction value (from the sum of the six lines) is $E(B-V)_{\mathrm{host}} = 0.085^{+0.017}_{-0.014}$ mag.

This is a surprisingly high value given the already very blue observed colors of SN 2021yja (see Section 3.1). To confirm this measurement, we also measure the equivalent width of the diffuse interstellar band (DIB) at 578 nm. From Equation (6) of Phillips et al. (2013), which can be rewritten

$$W_\lambda = (0.059^{+0.039}_{-0.024}\ \mathrm{nm\ mag^{-1}})\,E(B-V) \quad (1)$$

using the extinction law of Schlafly & Finkbeiner (2011), we would expect an equivalent width of $W_\lambda = 0.0050^{+0.0033}_{-0.0020}$ nm.

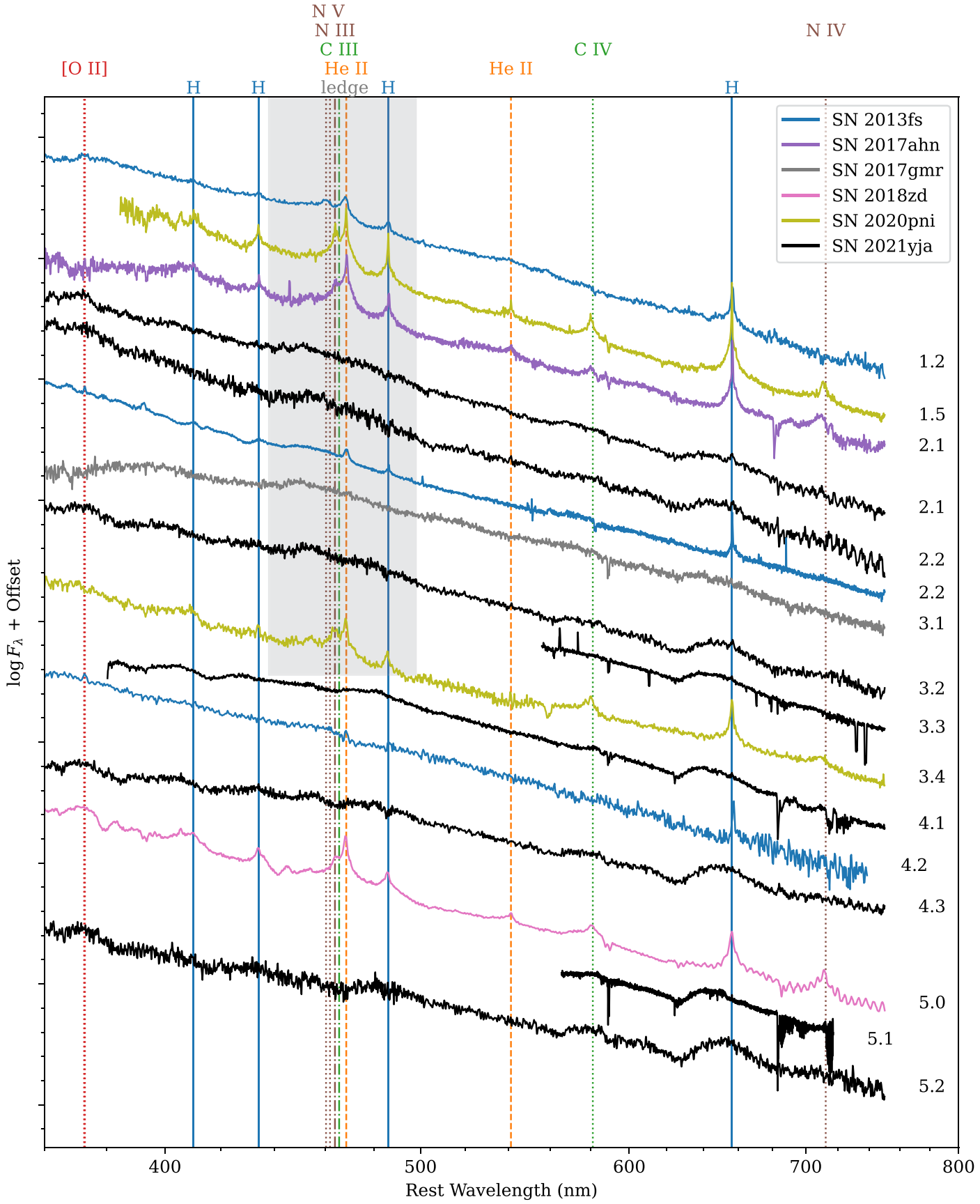

Figure 2. The early spectroscopic evolution of SN 2021yja compared to several other SNe II with good explosion constraints. The labels to the right of each spectrum give phase in rest-frame days after explosion, with uncertainties of 0.1–0.5 days. SN 2021yja does not show strong, narrow high-ionization lines like SNe 2013fs, 2017ahn, 2018zd, and 2020pni, an indication of short-lived circumstellar interaction. However, it does show broader features, including a mysterious broad feature around 450 nm (labeled "ledge") denoted by a gray bar, also seen in SN 2017gmr.

(The data used to create this figure are available.)

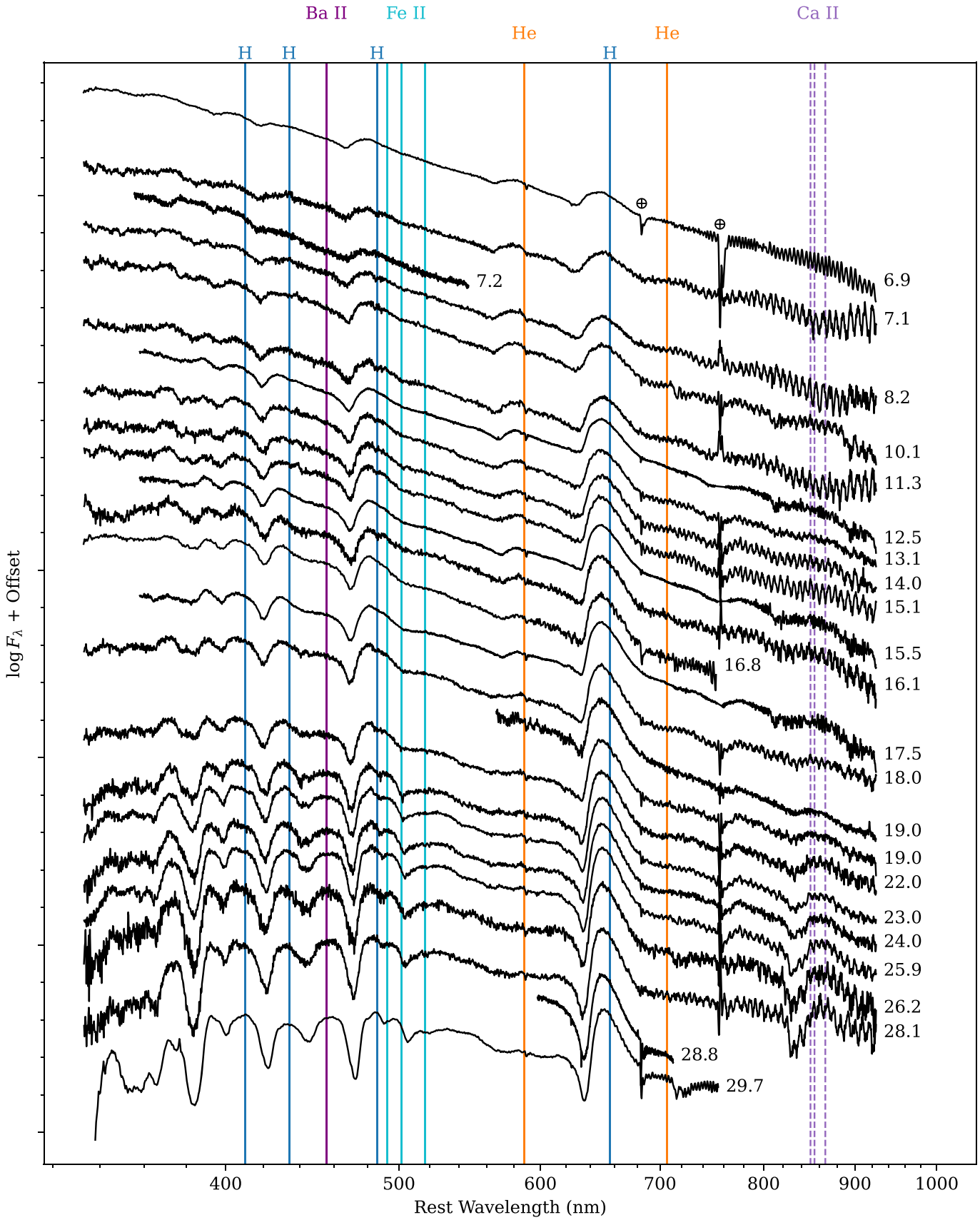

Figure 3. The spectroscopic evolution of SN 2021yja > 6 days after explosion, with colored lines at the rest wavelengths of selected features. (The data used to create this figure are available—See Figure 2.)

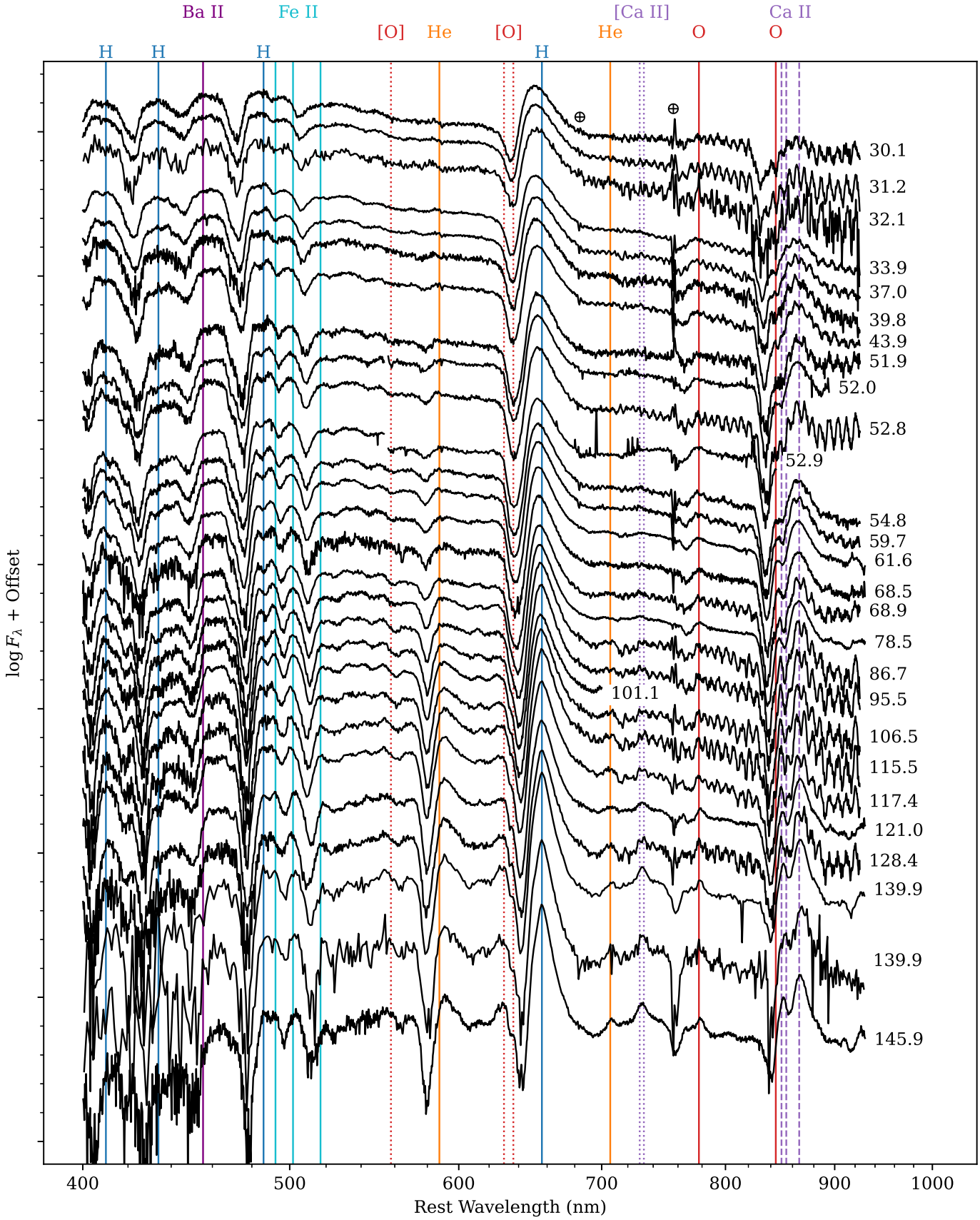

Figure 3. (Continued.)

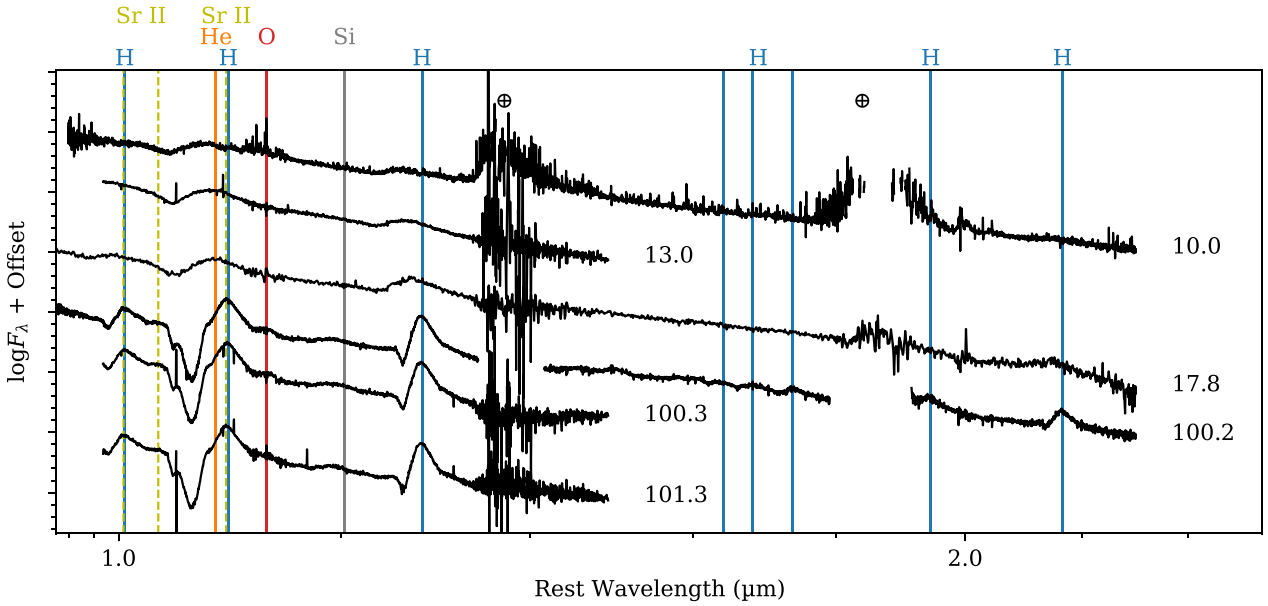

Figure 4. Near-infrared spectra of SN 2021yja. The weak helium absorption and the high-velocity helium feature in our > 100 d spectra indicate that SN 2021yja belongs to the "weak" class of Davis et al. (2019). (The data used to create this figure are available—See Figure 2.)

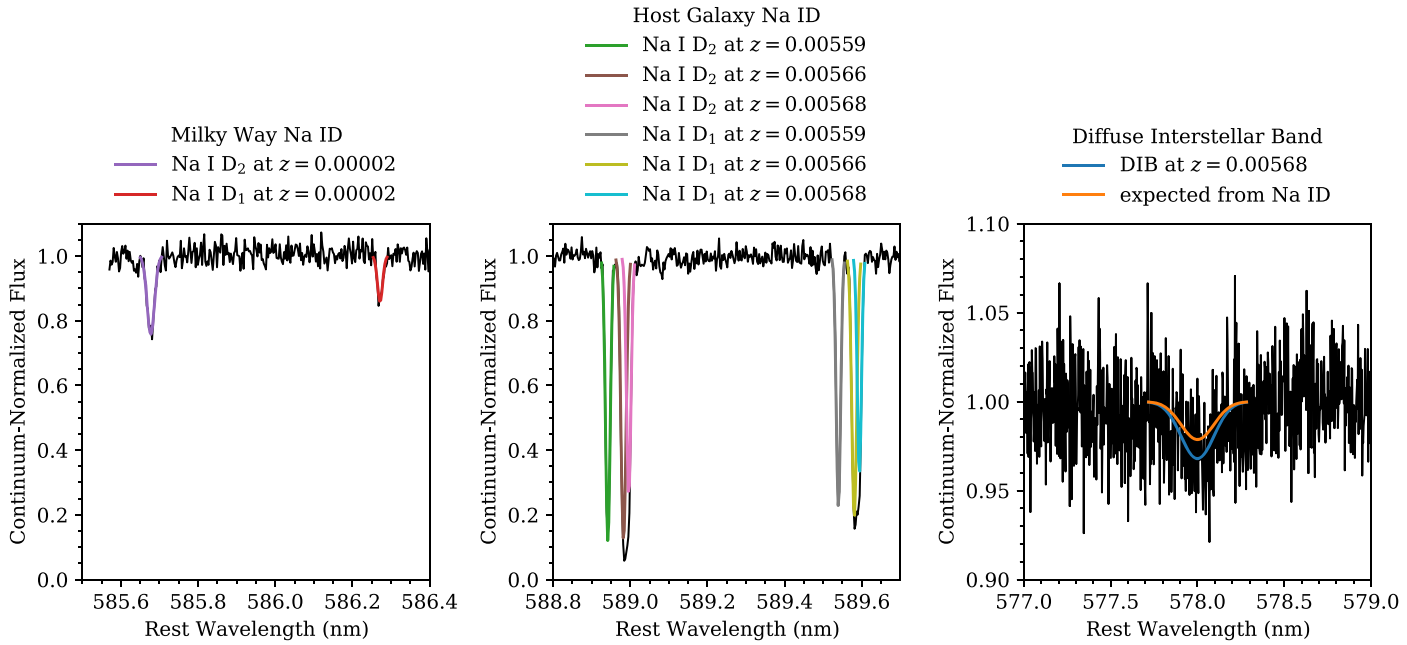

Figure 5. A high-resolution spectrum of SN 2021yja in the regions surrounding Na I D and the diffuse interstellar band (DIB) at 578 nm. The colored lines in the left and center panels indicate four distinct line-of-sight absorbers: one in the Milky Way ($z = 0.00002$) and three in the host galaxy ($z = 0.00559$, 0.00566, and 0.00568). Applying the relations of Poznanski et al. (2012), the Milky Way component is consistent with $E(B-V)_{\rm MW} = 0.0191$ mag from the dust maps of Schlafly & Finkbeiner (2011). The strong host galaxy components indicate an additional extinction of $E(B-V)_{\rm host} = 0.085^{+0.017}_{-0.014}$ mag, which is surprising given the blue observed colors of SN 2021yja. The DIB (right) confirms the significant extinction in the host galaxy. The blue Gaussian is a fit to the data, while the orange Gaussian shows the strength of DIB we would expect given the Na I D absorption, according to the extinction relation of Phillips et al. (2013). We adopt a total extinction of $E(B-V) = 0.104$ mag. (The data used to create this figure are available—See Figure 2.)

Due to the lower signal-to-noise ratio of this feature, we fit a Gaussian with a fixed center (578 nm at $z = 0.00568$) and width (FWHM = 0.222 nm; Tuairisg et al. 2000). Again integrating the best-fit Gaussian, we get an equivalent width consistent with our expectation, $W_\lambda = 0.0076$ nm. Given the more robust detection of the Na I D lines, we adopt the extinction derived above, for a total of $E(B-V) = 0.104$ mag, for which we correct using the extinction law of Fitzpatrick (1999). Note that this only accounts for interstellar extinction in the host galaxy, and not for any extinction due to CSM.

2.6. Distance

Distance estimates for NGC 1325 based on the method of Tully & Fisher (1977) listed on the NASA/IPAC Extragalactic Database range from 17.7 to 26.1 Mpc ($\mu = 31.24 - 32.09$ mag). For comparison, the redshift-dependent distance of NGC 1325 is

Table 1
Equivalent Widths

Line	Redshift	W_λ (nm)
DIB	0.00568	0.0076
D_2Na I	0.00002	0.0059
D_1Na I	0.00002	0.0024
D_2Na I	0.00559	0.0134
D_2Na I	0.00566	0.0148
D_2Na I	0.00568	0.0108
D_1Na I	0.00559	0.0111
D_1Na I	0.00566	0.0128
D_1Na I	0.00568	0.0091

23.6 ± 4.5 Mpc, assuming the cosmological parameters of the Planck Collaboration et al. (2020) and an uncertainty of $cz \approx 300\,\mathrm{km\,s^{-1}}$ due to the galaxy's peculiar velocity.

As an additional check on the SN distance, we apply the expanding photosphere method (EPM; Kirshner & Kwan 1974), which is a geometrical technique that can independently constrain the distance of an individual Type II SN. Assuming that the SN photosphere is expanding freely and spherically shortly after the explosion, we can derive the distance from the linear relation between the angular radius and the expanding velocity of the photosphere using the function

$$t = D\left(\frac{\theta}{v_{phot}}\right) + t_0 \tag{2}$$

where D is the distance, $v_{\rm phot}$ and θ are the velocity and angular radius of the photosphere, respectively, and t_0 is the explosion epoch. We estimate the photospheric velocity by measuring the minimum of the P Cygni profile of the Fe II line at 516.9 nm, which becomes detectable ~ 19 days after explosion. These measurements are listed in Table 2. In practice, the SN photosphere radiates as a dilute blackbody, so a dilution factor has to be involved when determining θ (Eastman et al. 1996; Hamuy et al. 2001; Dessart & Hillier 2005). We combine the multiband photometry to simultaneously derive the angular size (θ) and color temperature ($T_{\rm c}$) by minimizing the equation

$$\epsilon = \sum_{\nu \in S} \{m_\nu + 5log[\theta\xi(T_c)] - A_\nu - b_\nu(T_c)\}^2\,, \tag{3}$$

where ξ and b_ν are the dilution factor and the synthetic magnitude, respectively, both of which can be treated as a function of $T_{\rm c}$ (Hamuy et al. 2001; Dessart & Hillier 2005), A_ν is the reddening, m_ν is the observed magnitude, and S is the filter subset, i.e., $\{B, V\}$, $\{B, V, I\}$ and $\{V, I\}$. We use the dilution factors calculated by Jones et al. (2009) with the atmosphere model from Dessart & Hillier (2005). The best-fitting parameters D and t_0 in Equation (2) are estimated with a Markov Chain Monte Carlo (MCMC) method, and the priors of parameters are assumed to be uniform. The upper bound on the prior of t_0 is set to be MJD 59464.63, the first detection of the SN. Jones et al. (2009) showed that there is a clear departure from linearity between θ/v and $t \gtrsim 40$ days after explosion. Therefore, only data before this phase are used in our calculations (see Table 2). For the three filter subsets, we obtain distances of $24.0^{+2.5}_{-1.4}$ Mpc, $22.4^{+0.8}_{-0.5}$ Mpc, and $23.5^{+2.2}_{-1.3}$ Mpc, respectively. The explosion epochs are constrained to be $-2.2^{+1.7}_{-3.2}$ d, $-0.6^{+0.6}_{-1.0}$ d, and $-2.1^{+1.6}_{-3.0}$ d, respectively, relative to the estimate from our shock cooling model (see Section 3.2).

Seeing that these distances are consistent with the Tully-Fisher distance above, and given the large uncertainties from this method, we adopt the most recent Tully-Fisher estimate (calculated using the I band), $23.4^{+5.4}_{-4.4}$ Mpc ($\mu = 31.85 \pm 0.45$ mag; Tully et al. 2016). However, we keep in mind that all of our luminosity-dependent measurements suffer from a large systematic uncertainty in the distance.

3. Analysis

3.1. Bolometric Light Curve and Colors

For the purposes of constructing a bolometric light curve, we restrict ourselves to epochs where we have Swift observations, as UV photometry is critical for constraining the SED of young SNe. We supplement the Swift photometry with ground-based *griz* observations taken within 0.5 days of the Swift observation window. We fit a blackbody spectrum to the observed SED at each epoch using an MCMC routine implemented in the Light Curve Fitting package (Hosseinzadeh & Gomez 2020). This gives the temperature and radius evolution in the bottom panel of Figure 6. We then integrate the best-fit blackbody from the blue edge of the U band to the red edge of the I band to produce a pseudobolometric light curve, such that it will be comparable to pseudobolometric light curves in the literature. The top panel of Figure 6 compares the pseudobolometric light curve of SN 2021yja to 39 other SNe II from Valenti et al. (2016). SN 2021yja is among the most luminous.

A comparison with the light-curve model grid from Hiramatsu et al. (2021a) suggests that a hydrogen-rich envelope mass $\gtrsim 5\,M_\odot$ is required to reproduce the unusually long plateau duration (≈ 140 days). A higher explosion energy ($\gtrsim 2 \times 10^{51}$ erg) is also likely required to reproduce the plateau luminosity of SN 2021yja, which is higher than the models, suggesting an even more massive hydrogen-rich envelope according to light-curve scaling relations (e.g., Popov 1993; Kasen & Woosley 2009; Goldberg et al. 2019).

As suggested by Rubin & Gal-Yam (2017) and Kozyreva et al. (2020), the temperature evolution prior to the recombination phase can serve as a solid diagnostic of the progenitor radius. The temperature declines as a power law during this period and changes to a shallower decline after the onset of recombination (Nakar & Sari 2010; Shussman et al. 2016; Sapir & Waxman 2017; Faran et al. 2019), making this phase relatively easy to distinguish. In the bottom panel of Figure 6, we compare the temperature evolution of SN 2021yja to temperature models from Kozyreva et al. (2020) for various progenitor radii. We find that SN 2021yja lies between the $800\,R_\odot$ and $1000\,R_\odot$ models. Although there is no larger/hotter model, this comparison demonstrates that the progenitor of SN 2021yja is at least consistent with typical RSG radii ($100 - 1500\,R_\odot$; Levesque 2017), in contrast to our findings in Section 3.2.

We also downloaded UV light curves of all SNe II in the Swift Optical/Ultraviolet Supernova Archive (Brown et al. 2014). We correct these for Milky Way extinction only and plot them in Figure 7. SN 2021yja is the second most UV-luminous SN II observed by Swift, after only SN 2020pni (Terreran et al. 2022).

Lastly, in Figure 8, we compare the optical colors of SN 2021yja to a sample of other SNe II (Hamuy et al. 2001;

Table 2
Data and Results for the Expanding Photosphere Method

Phase (d)	Fe II Velocity (Mm s^{-1})	B (mag)	V (mag)	I (mag)	BV		BVI		VI	
					θ/v (Mpc^{-1} d)	Temp. (K)	θ/v (Mpc^{-1} d)	Temp. (K)	θ/v (Mpc^{-1} d)	Temp. (K)
19.0	8.122 ± 0.389	14.733 ± 0.056	14.549 ± 0.062	14.256 ± 0.045	0.805 ± 0.127	11533^{+2103}_{-1500}	0.847 ± 0.068	10735^{+640}_{-573}	0.866 ± 0.123	10438^{+1308}_{-1004}
22.0	8.091 ± 0.161	14.894 ± 0.061	14.582 ± 0.054	14.201 ± 0.029	0.940 ± 0.100	9353^{+1260}_{-989}	0.990 ± 0.044	9213^{+395}_{-357}	1.015 ± 0.087	9258^{+759}_{-632}
23.0	7.747 ± 0.180	14.894 ± 0.061	14.548 ± 0.063	14.192 ± 0.028	1.032 ± 0.113	8907^{+1228}_{-942}	1.040 ± 0.047	9212^{+394}_{-356}	1.028 ± 0.103	9569^{+922}_{-758}
24.0	7.599 ± 0.161	14.901 ± 0.056	14.518 ± 0.058	14.178 ± 0.027	1.105 ± 0.104	8465^{+989}_{-788}	1.075 ± 0.045	9138^{+362}_{-333}	1.032 ± 0.100	9767^{+898}_{-744}
25.9	7.190 ± 0.139	15.012 ± 0.090	14.605 ± 0.067	14.213 ± 0.040	1.131 ± 0.136	8349^{+1412}_{-1035}	1.153 ± 0.063	8757^{+500}_{-447}	1.146 ± 0.124	9170^{+975}_{-785}
26.2	7.264 ± 0.142	15.022 ± 0.076	14.609 ± 0.066	14.210 ± 0.040	1.131 ± 0.123	8211^{+1192}_{-906}	1.154 ± 0.059	8646^{+445}_{-402}	1.145 ± 0.121	9093^{+942}_{-761}
28.1	7.220 ± 0.138	15.049 ± 0.076	14.614 ± 0.057	14.223 ± 0.037	1.159 ± 0.111	7968^{+1039}_{-806}	1.155 ± 0.056	8644^{+424}_{-383}	1.136 ± 0.109	9166^{+844}_{-696}
29.7	5.986 ± 0.177	15.148 ± 0.073	14.643 ± 0.054	14.170 ± 0.012	1.456 ± 0.125	7333^{+815}_{-655}	1.505 ± 0.059	7965^{+324}_{-263}	1.535 ± 0.106	8368^{+638}_{-485}
30.1	6.719 ± 0.115	15.166 ± 0.065	14.642 ± 0.054	14.169 ± 0.013	1.313 ± 0.101	7189^{+709}_{-593}	1.353 ± 0.037	7861^{+249}_{-232}	1.368 ± 0.090	8370^{+649}_{-488}
31.2	6.312 ± 0.111	15.240 ± 0.080	14.658 ± 0.058	14.181 ± 0.018	1.439 ± 0.122	6791^{+756}_{-613}	1.449 ± 0.048	7728^{+322}_{-275}	1.452 ± 0.104	8340^{+699}_{-521}
32.1	6.041 ± 0.093	15.202 ± 0.076	14.625 ± 0.059	14.193 ± 0.026	1.524 ± 0.126	6813^{+734}_{-596}	1.485 ± 0.052	7924^{+317}_{-292}	1.447 ± 0.114	8723^{+710}_{-592}
33.9	6.093 ± 0.096	15.317 ± 0.070	14.696 ± 0.056	14.131 ± 0.033	1.508 ± 0.114	6499^{+606}_{-508}	1.613 ± 0.054	7131^{+252}_{-233}	1.670 ± 0.101	7578^{+511}_{-440}
37.0	5.659 ± 0.089	15.401 ± 0.061	14.684 ± 0.051	14.162 ± 0.029	1.734 ± 0.116	5938^{+444}_{-384}	1.729 ± 0.052	7045^{+214}_{-202}	1.713 ± 0.102	7908^{+498}_{-441}
39.8	5.553 ± 0.075	15.516 ± 0.067	14.757 ± 0.054	14.195 ± 0.028	1.749 ± 0.125	5736^{+448}_{-391}	1.766 ± 0.049	6809^{+212}_{-197}	1.776 ± 0.098	7598^{+475}_{-420}

(This table is available in machine-readable form.)

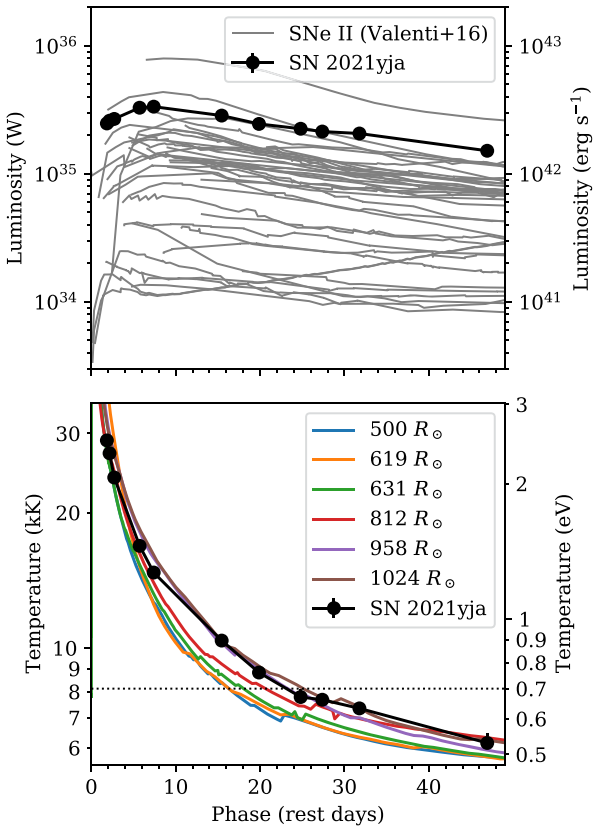

Figure 6. Top: Pseudobolometric light curve of SN 2021yja (black) compared to a sample of 39 pseudobolometric light curves from Valenti et al. (2016). Bottom: Evolution of the blackbody temperature of SN 2021yja compared to temperature evolution models of Kozyreva et al. (2020). SN 2021yja lies between the models with progenitor radii of 800 $R_\odot$ and 1000 $R_\odot$, although no model is significantly hotter than SN 2021yja. Note that the blackbody temperature does not cool below the hydrogen recombination threshold (~ 0.7 eV; dotted line) for several weeks, seemingly inconsistent with the appearance of strong hydrogen P Cygni lines after the first few days. This becomes relevant for the validity of our shock cooling model (Section 3.2).

(The data used to create this figure are available.)

Leonard et al. 2002; Elmhamdi et al. 2003; Bose et al. 2013; Munari et al. 2013; Anderson et al. 2014; Brown et al. 2014; Dall'Ora et al. 2014; Faran et al. 2014; Galbany et al. 2016; Rubin et al. 2016; Hosseinzadeh et al. 2018; de Jaeger et al. 2019; Szalai et al. 2019; Andrews et al. 2019; Bostroem et al. 2020; Dong et al. 2021; Terreran et al. 2022). The evolution is fairly typical, starting near the minimum colors for a hot blackbody, then evolving redward, with an inflection point around 15 days after explosion. In the terminology of Anderson et al. (2014), this is the transition time $t_{\rm tran}$ when the light-curve slope changes from s_1 (the initial decline) to s_2 (the "plateau"; see their Figure 1). Notably, we observe this transition in the colors even though the bolometric light curve in Figure 6 does not have a significant inflection point. We discuss this further in Section 4.1.

3.2. Shock Cooling Model

In the absence of circumstellar interaction, the early light curves of CCSNe are dominated by shock cooling emission, which depends upon the parameters of the explosion and the progenitor star, in particular the progenitor radius. We fit the model of Sapir & Waxman (2017) to the early light curve of SN 2021yja using the MCMC routine implemented in the Light Curve Fitting package (Hosseinzadeh & Gomez 2020). Because of the large uncertainties in extinction and distance outlined above, we allowed these to be free parameters in our model, with Gaussian priors according to their known values. We also included an intrinsic scatter term, σ, such that the effective uncertainty on each point is increased by a factor of $\sqrt{1+\sigma^2}$, with a half-Gaussian prior. This allows us to capture additional uncertainties, e.g., from photometric calibration, deviations from a blackbody spectrum, or small variations around the model, in our reported parameter uncertainties. The prior shapes and limits are given in Table 3. We ran 100 walkers for 1000 steps to reach convergence, assessed via visual inspection of the chain history, and for an additional 1000 steps to sample the posterior. Figure 9 shows the best-fit light curve, as well as the posterior distributions of and correlations between each parameter.

Qualitatively, the model fits SN 2021yja reasonably well across all bands. Unlike for several recent SNe II that have a significant peak in their early light curve (see, e.g., Hosseinzadeh et al. 2018), the shock cooling model is able to reproduce the smooth rise to plateau over ~ 10 days in the reddest bands. The model is nominally valid until MJD 59496.3 (31.7 days after explosion), at which point the temperature drops below 0.7 eV and recombination breaks the assumption of constant opacity (Sapir & Waxman 2017). This phase is roughly consistent with the recombination limit we estimated in Figure 6. However, there are clear hydrogen features in the spectra starting around 10 days, implying that recombination is occurring much earlier than this. For this reason, we do not fit our light curve after maximum light in the reddest bands (i.e., we only fit the data shown in Figure 9). This inconsistency in recombination time is one clue that the physics behind the shock cooling model may not completely describe the data, despite the appearance of a good fit.

Putting this concern aside for the moment, the model is most sensitive to the progenitor radius. The best-fit progenitor radius is $2030^{+260}_{-230}\,R_\odot$, which is significantly larger than typical RSG radii ($100-1500\,R_\odot$; Levesque 2017), and larger than the radius we infer in Section 3.1. Inspecting the correlations in Figure 9, we see that the radius estimate is strongly (positively) correlated with the extinction estimate. In other words, if we decrease our adopted extinction by $1-2\sigma$, we would estimate a more reasonable radius. However, we performed a second fit with a uniform prior in $E(B-V)$ and derived a best-fit extinction value similar to that in Section 2.5. (As Sapir & Waxman 2017 assume a blackbody SED in their model, this is equivalent to determining the extinction required to redden a blackbody into the observed SED.) Alternatively, as we discuss further in Section 4.1, the extreme UV flux may be the effect of circumstellar interaction on our light curve, which is not included in the shock cooling model. If we could model this interaction component separately, a smaller radius might be required to generate the shock cooling component. We can treat our best-fit radius as a robust upper limit on the true progenitor radius, though admittedly it is not very constraining.

We also find a best-fit explosion (shock-breakout) time of MJD 59464.40 ± 0.06, a mere 5.4 ± 1.4 rest-frame hours before our serendipitous detection with MuSCAT3. One

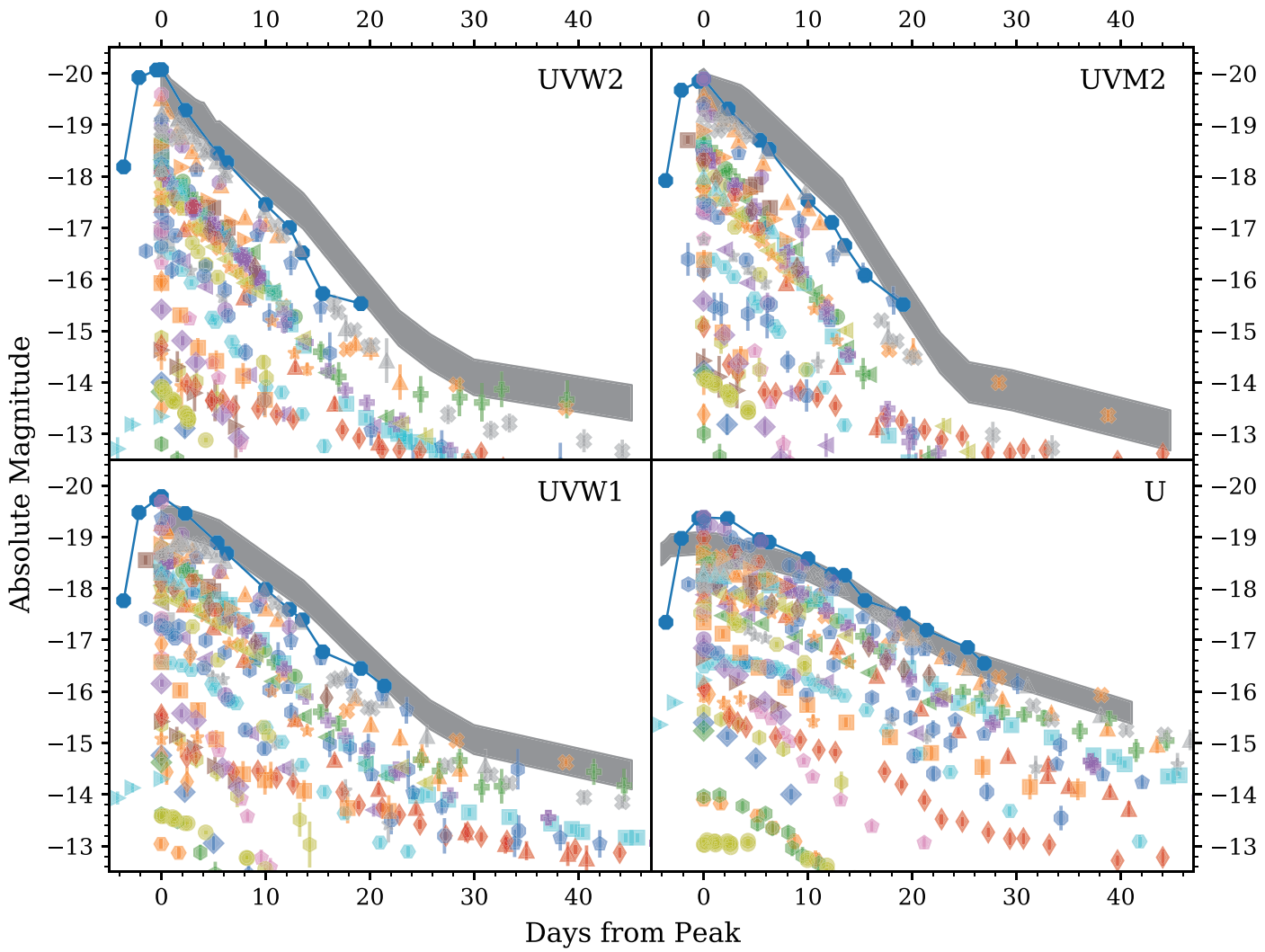

Figure 7. The UV light curve of SN 2021yja (shaded gray) compared to all SNe II in the Swift Optical/Ultraviolet Supernova Archive (colored points; corrected for Milky Way extinction only; Brown et al. 2014). All Swift data are in Vega magnitudes. The top of the gray region corresponds to $E(B-V)_{\rm host} = 0.085^{+0.017}_{-0.014}$ mag, whereas the bottom is only corrected for Milky Way extinction. This makes SN 2021yja the second most UV-luminous SN II observed by Swift, after SN 2020pni (blue octagons; Terreran et al. 2022). This unusually high UV luminosity suggests circumstellar interaction.

possibility, first suggested by Kilpatrick (2021), is that this first detection is of the progenitor prior to shock breakout. Indeed the absolute magnitude at this phase ($M_r = -11.5$ mag, $M_i = -11.3$ mag) is similar to the "precursor emission" of SN 2020tlf observed by Jacobson-Galán et al. (2022). To investigate this possibility, we performed the light-curve fit again without this first detection. The best-fit explosion time is still before the MuSCAT3 detection, and the model has a slightly larger intrinsic scatter ($\sigma \approx 5.8$). In the absence of extraordinary proof to the contrary, we conclude that this detection was after explosion and adopt the explosion time above as phase = 0 throughout our figures.

3.3. Nickel Mass

Near the end of our observations presented here, as of around 138 rest-frame days after explosion, the light curve of SN 2021yja has settled on the radioactive-decay tail, where the ^{56}Co → ^{56}Fe decay provides most of the input power. We confirm that the bolometric decline rate over the last four epochs of photometry from Las Cumbres Observatory is 0.0096 mag day^{-1}, very close to the ^{56}Co → ^{56}Fe decay rate (0.0098 mag day^{-1}; Colgate & McKee 1969). During this phase, we can measure the mass of radioactive ^{56}Ni produced in the explosion by scaling the luminosity to that of SN 1987A, which had an independent ^{56}Ni measurement ($M_{\rm Ni,87A} = 0.075\,M_\odot$; Spiro et al. 2014; Valenti et al. 2016).

We calculate the bolometric luminosity for these four epochs by directly integrating the SED over the U to i filters. This is different than the blackbody-fitting method we used during the photospheric phase, because at these late times the SED is no longer described by a Planck (1906) function (e.g., Martinez et al.2022). We calculate a bolometric light curve of SN 1987A with the same method using photometry from Catchpole et al. (1988) via the Open Supernova Catalog (Guillochon et al. 2017), interpolate to the four epochs of SN 2021yja photometry, and take the average ratio. We find that SN 2021yja produced $M_{\rm Ni} = 0.141^{+0.074}_{-0.049}\,M_\odot$, where the uncertainty is dominated by our distance uncertainty. This places SN 2021yja at the 97th percentile for nickel mass among SNe II (Anderson 2019), although we caution that this measurement is only $\approx 1.6\sigma$ above the nickel mass of SN 1987A. Another possibility is that our measurement is inflated by extra